

Adaptive signal decomposition based on wavelet ridge and its application



Yi Qin ^{a,b,*}, Baoping Tang ^a, Yongfang Mao ^c

^a State Key Laboratory of Mechanical Transmission, Chongqing University, Chongqing 400044, People's Republic of China

^b School of Manufacturing Science and Engineering, Sichuan University, Chengdu 610065, People's Republic of China

^c College of Automation, Chongqing University, Chongqing 400044, People's Republic of China

ARTICLE INFO

Article history:

Received 6 January 2015

Received in revised form

22 September 2015

Accepted 26 September 2015

Available online 23 October 2015

Keywords:

Accurate decomposition

Noise sensitivity

Nonstationary vibration

Complex Morlet wavelet

Mechanical fault diagnosis

ABSTRACT

Signal decomposition is a widely-used approach for multicomponent signal processing. To improve the accuracy and anti-noise performance of multicomponent decomposition, this paper proposes a novel multicomponent signal decomposition method based on wavelet ridge extraction, called the Wavelet ridge signal decomposition (WRSD). A wavelet ridge extraction algorithm is introduced. We find that this algorithm can obtain the wavelet ridge of one component in a multicomponent signal and the initial scale will determine the wavelet ridge of which component is extracted. Since the instantaneous frequency obtained by wavelet ridge has small frequency fluctuation, low-pass filtering is used to increase the accuracy of instantaneous frequency estimation. With the improved instantaneous frequency, the synchronous demodulation method is used to separate the corresponding component from the signal composition. By repeating this process, all components can be adaptively and automatically obtained. This method is employed to analyze three typical simulated vibration signals and compared with Hilbert vibration decomposition and empirical mode decomposition. The comparison results demonstrate its superiority in decomposition accuracy and noise insensitivity. Finally, the proposed WRSD method is successfully applied to the diagnosis of a shaft misalignment fault and a gearbox wear fault.

© 2015 Elsevier B.V. All rights reserved.

1. Introduction

In nature and engineering, there are many multicomponent signals, and most of these signals are nonstationary. Various signal processing methods have been proposed to analyze the multicomponent signals, such as short time Fourier transform (STFT) [1], Wigner-Ville distribution (WVD) [2], wavelet scalogram [3], iterative Hilbert transform [4], etc. A better way to reveal the time-varying amplitude and frequency characteristic is to decompose the multicomponent

signal into monocomponent signals firstly, and then do further analysis with these decomposed components. Signal decomposition technology has been successfully applied to various fields, such as mechanical fault diagnosis [5,6], system identification [7], image texturing [8], biological data processing [9], etc.

In the past three decades, signal decomposition has been a hot point for signal processing research, and many effective methods have been proposed. The discrete wavelet transform was early used to decompose the signal [10]. But the frequency resolution at each scale is coarse due to the dyadic time-frequency grid. To improve the time-frequency resolution, overcomplete wavelet transform has been widely researched. For example, higher density wavelet transform [11] and dense framelet transform [12] have been successfully

* Corresponding author at: State Key Laboratory of Mechanical Transmission, Chongqing University, Chongqing 400044, People's Republic of China. Tel./fax: +86 2365105721.

E-mail address: qy_808@aliyun.com (Y. Qin).

applied to the analysis of mechanical faulty vibration signal. A powerful approach, named as empirical mode decomposition (EMD), was proposed by Huang et al. [13]. This method has been widely applied to various fields including mechanical engineering, structural engineering, biomedicine, etc. However, EMD has the problem of mode mixing [14], which limits its frequency resolution. Recently, another multi-component decomposition method, called Hilbert vibration decomposition (HVD), was proposed by Feldman [15]. HVD has good frequency resolution and can distinguish various narrowband components while EMD cannot. However, both EMD and HVD are sensitive to additive random noise. They cannot extract low level signals from the large amplitude additive noise [16]. Like HVD, analytical mode decomposition (AMD) based on Hilbert transform was developed by Chen and Wang [17], which can separate closely spaced frequency components. Generalized demodulation time-frequency method and its improved methods are also proposed to process nonlinear multicomponent signals [18–20]. These methods have fine resolution, but it is very important to select the appropriate phase functions. More recently, sparse decomposition based on different transform basis was proposed by Qin [21], which has high decomposition accuracy, but its computation speed is relatively slow. We usually expect that the signal decomposition method is automatic, adaptive, accurate and of low noise sensitivity. With this motivation, a new multicomponent signal decomposition approach based on wavelet ridge is explored in this paper.

It is well-known that wavelet transform has good time-frequency localization property. Via wavelet ridge, the signal frequency can be well obtained. An adaptive wavelet ridge computation algorithm was proposed by Delprat et al. [22]. This algorithm is mainly used to analyze monocomponent signals, whereas it can also extract the wavelet ridge of one component of a multicomponent signal, and we find that the initial scale will determine the wavelet ridge of which component is extracted and its theoretical explanation is given. After obtaining one component's instantaneous frequency, the classic synchronous demodulation technique is used to reconstruct this component. Then this component is subtracted from the signal composition. By repeating this process, all components can be extracted. The decomposition process is adaptive, automatic and can obtain the high frequency component successively. In this study, the proposed method is named as Wavelet ridge signal decomposition (WRSD). Compared with commonly-used multicomponent decomposition methods, the proposed WRSD method has higher decomposition accuracy and is less sensitive to random noise with low intensity. The application results also show that the proposed method can better extract the weak fault feature from the mechanical vibration signals.

2. Wavelet ridge theory

2.1. Asymptotic signal and its exponential model

Let us first briefly revisit the basic definitions and properties of asymptotic signals. An arbitrary real energy signal $s(t)$ can be represented in terms of instantaneous

amplitude $A(t)$ and phase $\phi(t)$, i.e. in the following form:

$$s(t) = A(t) \cos(\phi(t)) \quad (1)$$

where $A(t) \geq 0$ and $\phi(t) \in [0, 2\pi]$. Obviously, such a representation is not unique. Via Hilbert transform, it is convenient to specify a particular one. The analytic signal $Z_s(t)$ associated with $s(t)$ is obtained by Hilbert transform, which can be expressed as

$$Z_s(t) = (1 + iH)s(t) = A_s(t)\exp(i\phi_s(t)) \quad (2)$$

where H denotes the Hilbert transform.

Particularly assume that $s(t)$ is asymptotic, which essentially means that

$$\left| \frac{d\phi}{dt} \right| \gg \left| \frac{1}{A} \frac{dA}{dt} \right| \quad (3)$$

Then the instantaneous frequency of $s(t)$ can be calculated as

$$f_s(t) = \frac{1}{2\pi} \frac{d\phi_s}{dt} \quad (4)$$

2.2. Ridge and wavelet curves

By wavelet transform, we can also describe the time-varying frequency characteristic of the signal. Assuming that the signal and the wavelets are all asymptotic, with the stationary phase method, we can get some particular sets of curves in the time-scale half-plane, namely the ridge and the wavelet curve. The ridge describes instantaneous frequency characteristic of the signal.

Let $\psi(t)$ be an asymptotic analytic wavelet [22], which is expressed as

$$\psi(t) = A_\psi(t)\exp[i\phi_\psi(t)] \quad (5)$$

With this mother wavelet, the wavelet transform of $Z_s(t)$ is given by

$$W_z(a, b) = \frac{1}{\sqrt{a}} \int_{-\infty}^{\infty} Z_s(t) \psi^* \left(\frac{t-b}{a} \right) dt \\ = \frac{1}{\sqrt{a}} \int_{-\infty}^{\infty} A_s(t) \exp[i\phi_{a,b}(t)] dt \quad (6)$$

where a and b are respectively scale parameter and shift parameter, $\phi_{a,b}(t)$ and $A_{a,b}(t)$ are respectively given by

$$\phi_{a,b}(t) = \phi_s(t) - \phi_\psi \left(\frac{t-b}{a} \right) \quad (7)$$

$$A_{a,b}(t) = A_s(t) \exp \left(\frac{t-b}{a} \right) \quad (8)$$

The stationary point t_s is defined as $\phi'_{a,b}(t_s) = 0$, i.e.

$$\phi'_s(t_s) = \frac{1}{a} \phi'_\psi \left(\frac{t_s-b}{a} \right) \quad (9)$$

We can see from Eq. (9) that the stationary point t_s is the function of (a, b) .

Then the ridge is defined to be the set of points (a, b) such that $t_s(a, b) = b$. It immediately follows from Eq. (9) that on the ridge

$$a = a_r(b) = \frac{\phi'_\psi(0)}{\phi'_s(b)} \quad (10)$$

The wavelet curve is defined to be the connected component of $(a_r(b_0), b_0)$ of the set of points $(a, b) \in \mathbf{R}^2$ such that $t_s(a, b) = b_0$ and

$$\phi'_\psi \left(\frac{b_0 - b}{a} \right) = \frac{a}{a_r(b_0)} \phi'_\psi(0) \quad (11)$$

It then follows from Eq. (11) that the wavelet curve is uniquely determined by the mother wavelet. We usually use real symmetric window function and complex sinusoid function to construct the asymptotic analytic wavelet, which is expressed as

$$\psi(t) = g(t) \exp(i\omega_0 t) \quad (12)$$

where ω_0 is the central frequency of $\psi(t)$ and $\omega_0 = \phi'_\psi(0)$. It immediately follows from Eqs. (4) and (10) that the instantaneous frequency of $s(t)$ at the instant t is given by

$$f_s(t) = \frac{1}{2\pi} \times \frac{\omega_0}{a_r(t)} \quad (13)$$

2.3. Ridge extraction algorithm

The phase information of complex wavelet transform can be used to extract the ridge. Let $\varphi(a, b)$ be the phase of the wavelet coefficient $[W_z(a, b)]$, i.e. $\varphi(a, b) = \arg [W_z(a, b)]$. For a given wavelet curve, on its intersection with the ridge, the phase $\varphi(a, b)$ has the following other property

$$\left. \frac{\partial \varphi(a, b)}{\partial b} \right|_{t_s(a, b) = b_0} = \frac{1}{a} \phi'_\psi \left(\frac{t_s - b}{a} \right) + \left[\frac{\partial a}{\partial b} \right] \frac{t_s - b}{a^2} \phi'_\psi \left(\frac{t_s - b}{a} \right) = \frac{\phi'_\psi(0)}{a} \quad (14)$$

This equation provides an approach for the ridge extraction [22]. To avoid the divergence in the computation process, an improved wavelet ridge extraction algorithm will be used in this paper. For a discrete time signal $s(k)$, the steps of this algorithm are summarized as follows:

- 1) Choose a family of asymptotic analytic wavelets with the central frequency ω_0 . Set the maximum iterative number i_{max} (it can be set as 10), iterative thresholding ϵ (it can be set as 0.005), and initial scale a_0 . Let $a = a_0$, $\epsilon_{min} = \epsilon$, $k = 0$, and $i = 0$.
 - 2) Calculate the analytic signal $Z_s(k)$ by Eq. (2).
 - 3) Calculate the wavelet coefficients $W_z(a, k)$ and $W_z(a, k+1)$ of $Z_s(k)$ and $Z_s(k+1)$ respectively, then calculate their corresponding phase $\varphi(a, k)$, $\varphi(a, k+1)$.
 - 4) Calculate
- $$a_1 = \frac{\omega_0}{D_b \varphi(a, k)} = \frac{\omega_0}{\varphi(a, k+1) - \varphi(a, k)} \quad (15)$$
- 5) Calculate $e = |(a_1 - a)/a|$. If $e < \epsilon$, let $a_r(k) = a$, and go to the next step; otherwise, let $a = a_1$, and if $e < \epsilon_{min}$, then let $\epsilon_{min} = e$, $a_{min} = a$, $i = i + 1$. If $i < i_{max}$, repeat steps 2)–4), otherwise let $a_r(k) = a_{min}$ and go to the next step.
 - 6) Let $k = k + 1$, $i = 0$, and $\epsilon_{min} = \epsilon$, repeat steps 2)–5), until all data are processed.

After obtaining the wavelet ridge, the instantaneous frequency of signal can be calculated by Eq. (13).

In this paper, we will use the complex Morlet wavelet for ridge extraction, which is defined as

$$\psi(t) = \frac{1}{\sqrt{2\pi}} \exp \left(-\frac{t^2}{2} \right) \exp(i\omega_0 t) \quad (16)$$

Although increasing the central frequency ω_0 may improve the frequency resolution of the decomposition, it does harm to the IF estimation of sinusoidal frequency modulation signals, so the central frequency should not be too large. From many experiments, we find that the central frequency can be set between 2π and 4π . In this range, for the most typical mechanical vibration signals, the IFs obtained by different central frequencies have a little difference. Indeed, optimizing the wavelet parameter will increase the accuracy of IF estimation according to the analyzed signals, but it is not the key point of this paper. In the following examples, we just choose a fixed central frequency in the range of $[2\pi, 4\pi]$ in advance, but the decomposition results are also satisfied.

3. Property of wavelet ridge extraction for multi-component signal

3.1. Experimental results

The improved wavelet ridge extraction algorithm can be well used to compute the instantaneous frequencies of monocomponent signals. What will happen if this algorithm is applied to process noisy multicomponent signals?

Let us consider a noisy two-component sinusoidal signal

$$s(t) = 0.6 \cos(2\pi \times 30t) + \cos(2\pi \times 60t) + n_s(t) \quad (17)$$

where $n_s(t)$ is a Gaussian white noise with the standard deviation of 0.3. Let the sampling frequency and the data length be 500 Hz and 1024, respectively. The waveform of this harmonic signal is illustrated in Fig. 1.

In this simulation, let central frequency ω_0 be 4π . Firstly, we set a_0 as 25.5. The improved wavelet ridge extraction algorithm is employed to analyze the noisy signal, and the obtained result is illustrated in Fig. 2. It can be seen from Fig. 2 that the instantaneous frequency of the low frequency component is effectively calculated, but there exists an end effect and frequency fluctuation. Then, if we decrease a_0 from 25.5 to 3.3, the obtained result is illustrated in Fig. 3. From this figure, we can see that the instantaneous frequency of the high frequency component is obtained, but there also exists an end effect and frequency fluctuation. To overcome the end effect, symmetric extension method can be employed to process the initial signal.

Consequently, it can be known from these two simulated tests that the initial scale a_0 will determine the wavelet ridge of which component is extracted. Especially when the amplitude of high frequency component is larger than that of low frequency component or their amplitudes are close to each other, using the small initial scale will obtain the instantaneous frequency of the high frequency component while using the large initial scale will obtain the instantaneous frequency of the low frequency

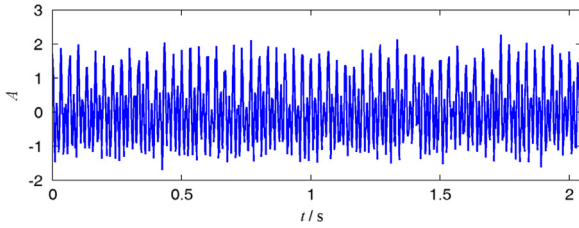


Fig. 1. The waveform of a noisy two-component sinusoidal signal.

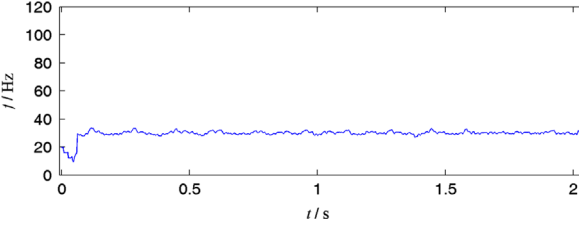


Fig. 2. The instantaneous frequency of the low frequency component for large initial scale.

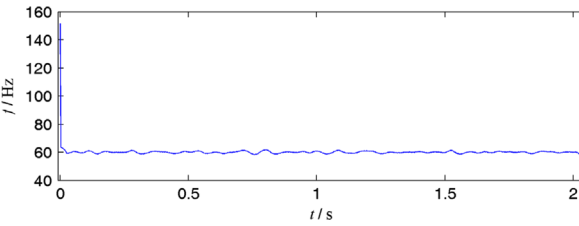


Fig. 3. The instantaneous frequency of the high frequency component for small initial scale.

component. Moreover, since the noise energy is dispersed in the whole wavelet domain and wavelet transform has good time–frequency localization property, this algorithm has better anti-noise performance compared to the method based on Hilbert transform (or Teager energy operator), which is highly sensitive to noise even though its intensity is quite small. It can be also seen from Figs. 2 and 3 that there are small frequency fluctuations. To further improve the accuracy of IF estimation, the frequency fluctuation should be removed by zero-phase low-pass FIR filtering. Suppose that $x(n)$ and $h(n)$ respectively denote the input discrete signal and FIR filter, zero-phase digital filtering can be performed by

$$\begin{cases} y_1(n) = x(n) * h(n) \\ y_2(n) = y_1(N-1-n) \\ y_3(n) = y_2(n) * h(n) \\ y(n) = y_3(N-1-n) \end{cases} \quad (18)$$

where $*$ denotes the convolution operator, $y(n)$ denotes the output discrete signal and N is the data length. Obviously, there are two convolution operations in zero-phase digital filtering, thus the side-effect will occur. The IF component shown in Fig. 3 will be used to demonstrate the side-effect of zero-phase low-pass FIR filtering. To avoid the interruption of the false IF data near the end, we just use the IF data at the time interval [0.01 2.044] s for digital filtering. The normalized Remez filter cut-off

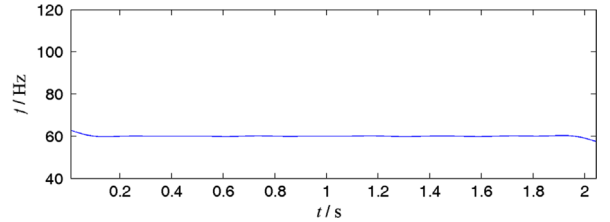


Fig. 4. The filtered IF of the high frequency component.

frequency is set as 0.02. After zero-phase low-pass FIR filtering, the filtered IF component is illustrated in Fig. 4. From this figure, we can see the clear end swing phenomenon at the two sides. It again illustrates that data extension is extremely necessary.

As we know, for harmonic signal, chirp signal and sinusoidal amplitude modulation and phase modulation signal, the maximum frequency of the ideal IF component (constant IF or time-varying IF) is usually quite small, and it is lower than the frequency of the fluctuation. Thus by setting a small filter cut-off frequency can effectively remove the frequency fluctuation. Via many numeric experiments, it can be also proven that the zero-phase low-pass FIR filtering can be well applied to remove the frequency fluctuations of the constant IF components and the typical time-varying IF components.

Totally speaking, the improved wavelet ridge extraction algorithm can be well employed to obtain the instantaneous frequency of one component in the multi-component signal even though there is noise interference. However, the noise intensity cannot be too large, otherwise the IF may not be rightly obtained, in such case, signal denoising should be done first.

3.2. Theoretical analysis

Consider a simple two-component harmonic signal

$$s(t) = s_1(t) + s_2(t) = A_1 \cos(\omega_1 t) + A_2 \cos(\omega_2 t + \varphi) \quad (19)$$

where $\omega_1 > \omega_2$ with the asymptotic analytic wavelet, the wavelet transform of $s(t)$ can be calculated as

$$W_s(a, b) = A_1 \bar{G}(a\omega_1) e^{i\omega_1 b} + A_2 \bar{G}(a\omega_2) e^{i(\omega_2 b + \varphi)} = A_1 \bar{G}(a\omega_1) e^{i\omega_1 b} \left[1 + C(a) e^{i(\omega_2 - \omega_1)b + i\varphi} \right] \quad (20)$$

where $G(\omega)$ denotes the Fourier transform of $g(t)$ and

$$C(a) = \frac{A_2 \bar{G}(a\omega_2)}{A_1 \bar{G}(a\omega_1)} \quad (21)$$

Let $\epsilon = |2\pi/(\omega_2 - \omega_1)|$ be a nonnegative real number, and define

$$T = n \left| \frac{2\pi}{\omega_2 - \omega_1} \right| + \epsilon \quad (22)$$

where n is a positive number. By the use of T , we define

$$\omega_a = \frac{1}{T} \int_{b_0}^{b_0+T} \frac{\partial \psi(a, b)}{\partial b} db \quad (23)$$

where $\psi(a, b)$ denotes the phase of $W_s(a, b)$. It is easy to note that ω_a is approximately equivalent to $D_b \varphi(a, k)$. In

such a simple case, a straightforward computation (see Appendix A) can be performed, and we can get that

$$\omega_a = \omega_1 + O(\epsilon/n) \quad \text{if } C(a) < 1 \quad (24)$$

$$\omega_a = \omega_2 + O(\epsilon/n) \quad \text{if } C(a) > 1 \quad (25)$$

It can be also directly seen from Eq. (20) that the phase $\psi(a, b)$ mainly depends on the phase of the first component when $C(a)$ is smaller, while $\psi(a, b)$ mainly depends on the phase of the second component when $C(a)$ is larger. Obviously, we can see from Eq. (21) that the value of $C(a)$ mainly depends on the scale parameter one started with. According to Eqs. (15), (24) and (25), it can be easily known that the IF extracted by the improved wavelet ridge extraction algorithm is highly related to the initial scale.

Specifically for the complex Morlet wavelet that given by Eq. (16), $C(a)$ can be explicitly written as

$$C(a) = \frac{A_2}{A_1} e^{-\frac{1}{2}a^2(\omega_2^2 - \omega_1^2)} \quad (26)$$

As $\omega_1 > \omega_2$, $C(a)$ will be smaller if a is smaller. It follows that the IF of the high frequency component $s_1(t)$ can be extracted with the small initial scale especially when $A_1 > A_2$. Through a great many of experiments, we also find that the IF of $s_1(t)$ can be probably extracted with a small initial scale even though A_1 is a little smaller than A_2 . On the contrary, if a large initial scale is set, the IF of the low frequency component $s_2(t)$ can be obtained by the improved wavelet ridge extraction algorithm.

4. Multicomponent decomposition based on wavelet ridge extraction

After obtaining the instantaneous frequency (IF) of one component, synchronous demodulation approach (its computation procedure can be seen in Ref. [23]) is used to calculate the corresponding phase and instantaneous amplitude (IA), and then reconstruct this component. To achieve the decomposition from high frequency component to low frequency component, the initial scale of the first decomposition stage should be set as a small value, and then the initial scale is increased gradually or kept the same at all stages. In order to avoid end effect and improve calculation accuracy, the increased initial scales are used in this paper. Based on the above principle, an adaptive multicomponent signal decomposition method is proposed, and its concrete steps are summarized as follows:

- 1) Suppose that $s(t)$ denotes the initial multicomponent signal. Perform symmetric extension on $s(t)$, chose a family of asymptotic analytic wavelets with the central frequency ω_0 , set the initial scale a_0 (it can be set as the value between 2 and 5), let $i=1$, and initialize $x(t)=s(t)$.
- 2) Perform the improved wavelet ridge extraction algorithm on $x(t)$ to obtain the ridge $a_r(t)$ of one component.
- 3) Calculated the IF estimation $f_e(t)$ by Eq. (13), then perform low-pass filtering on $f_e(t)$ (the normalized

cut-off frequency can be 0.02–0.04), and obtain the corrected IF $f_i(t)$.

- 4) With $f_i(t)$, use the synchronous demodulation approach to obtain the IA $A_i(t)$ and the corresponding component $x_i(t)$.
- 5) Calculate the stopping criterion.

$$SC = \frac{\sum_t x_i^2(t)}{\sum_t s^2(t)} \quad (27)$$

If SC is smaller than a threshold (it can be set as 0.05) or the number of the obtained components i equals the preset maximum decomposing number i_m , then stop the iteration; otherwise, subtract $x_i(t)$ from $x(t)$, i.e. $x(t)=x(t)-x_i(t)$, and let $i=i+1$, $a_0=1.2a_0$, then repeat steps (2)–(5).

We call this proposed signal decomposition method as Wavelet ridge signal decomposition (WRSD). Via WRSD, we obtain not only all monocomponent signals, but also their IFs and IAs. It is also worth noting that the decomposition result may not be from high frequency component to low frequency component because the initial scale is empirically set and increased. If we hope to get the desirable decomposition result, we can compute the mean value of each component's IF, and then rearrange all components. The flow chart of WRSD is briefly depicted as Fig. 5. In this figure, for simplicity and convenience, the symmetric extension step is omitted. The computational complexity of WRSD mainly comes from step (2). For the extraction of one wavelet ridge, its computational complexity can be estimated as $O(c \times N^2)$, where c represents the iterative number and N denotes the data length. It then follows that the computational complexity of the proposed method is approximate to $O(m \times c \times N^2)$ if there is m components.

Then let us discuss the frequency resolution and convergence behavior of WRSD. Consider such an arbitrary two-component signal that

$$f(t) = A_1(t) \cos \phi_1(t) + A_2(t) \cos \phi_2(t) \quad (28)$$

With the asymptotic analytic wavelet, the wavelet transform of $f(t)$ can be calculated as

$$W_f(a, b) = \frac{\sqrt{a}}{2} A_1(b) \exp[i\phi_1(b)] G(a[\xi - \phi'(b)]) + \frac{\sqrt{a}}{2} A_2(b) \exp[i\phi_2(b)] G(a[\xi - \phi'(b)]) \quad (29)$$

where $\phi'(b)$ denotes the first derivative of $\phi(b)$. In Eq. (29), we have neglected the correction term. It can be known from Ref. [10] that at the wavelet ridge $a=\omega_0/\phi'_1(b)$, if

$$G(a|\phi'_1(b) - \phi'_2(b)|) \ll 1 \quad (30)$$

then the second IF ϕ'_2 will not disturb the first IF ϕ'_1 . Let $\Delta\omega$ be the bandwidth of $G(\omega)$. To satisfy Eq. (30), the following inequality:

$$a|\phi'_1(b) - \phi'_2(b)| \geq \Delta\omega \quad (31)$$

should hold. It then immediately follows that

$$\frac{|\phi'_1(b) - \phi'_2(b)|}{\phi'_1(b)} \geq \frac{\Delta\omega}{\omega_0} \quad (32)$$

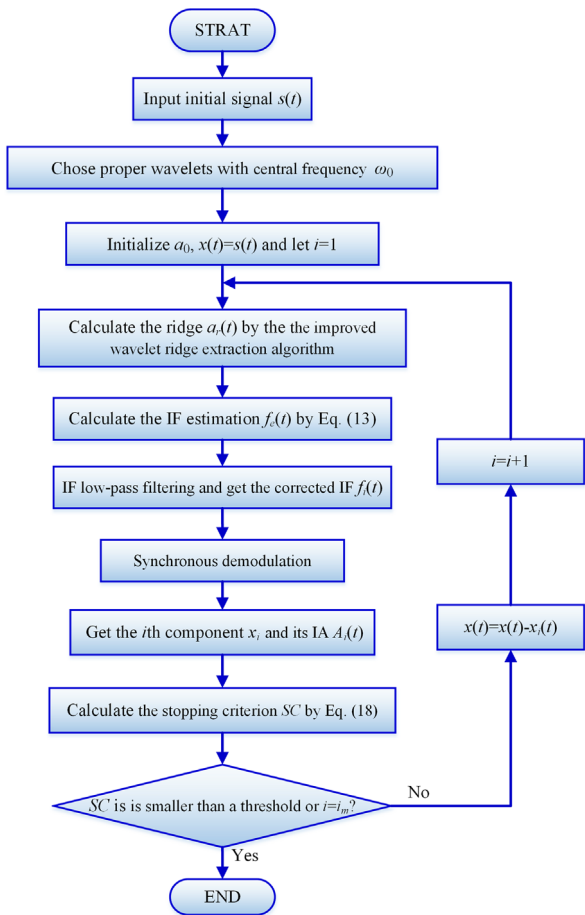


Fig. 5. The flowchart of the proposed vibration component separation algorithm.

From Eq. (32), we can know that the wavelet should have small $\Delta\omega/\omega_0$ in order to separate two close components. Obviously, by increasing ω_0 can improve the frequency resolution of WRSD. However, due to the numeric calculation error, the proposed algorithm is quietly difficult to achieve the ideal signal component separation.

If all the components can be rightly separated from the original signal, the WRSD algorithm must be convergent. However, once frequency aliasing occurs, the proposed method may not be convergent, thus it is necessary to set a maximum decomposing number. Moreover, via a large number of simulation experiment, it can be seen that the sample rate will not affect the effectiveness of the proposed decomposition algorithm, and the number of components also has little influence on the proposed WRSD algorithm owing to the high accuracy of each decomposition step. The simulated examples will be given in the next section.

5. Simulation test

In this section, we illustrate the effectiveness of the proposed WRSD method via four simulation examples. To

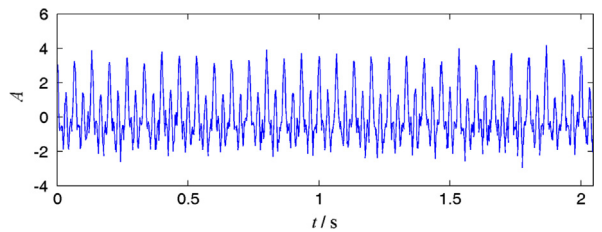


Fig. 6. The waveform of a noisy three-component harmonic signal.

demonstrate the advantage of WRSD, the random white noise is added in each experimental example, and the EMD method and HVD method are used for comparison.

5.1. Example 1

Multicomponent harmonic signals widely exist in mechanical systems and power systems. The WRSD method can be used for analyzing these signals to recognize the system state. Consider a noisy three-component harmonic signal

$$s(t) = \cos(2\pi \times 15t) + 1.4 \cos(2\pi \times 30t) + \cos(2\pi \times 60t) + n_s(t) \quad (33)$$

where $n_s(t)$ is a Gaussian white noise with the standard deviation of 0.3. The sampling frequency is 500 Hz, and the length of signal is 1024. The waveform of this noisy harmonic signal is illustrated in Fig. 6.

Firstly, the WRSD method is used to decompose this signal. The central frequency of the complex Morlet wavelet is chosen as 4π . The result of WRSD is shown in Fig. 7, and the errors between the original components and the obtained components are shown in Fig. 8. With the IFs and IAs of the obtained components, we can get the time-frequency spectrum of the decomposed result, which is shown in Fig. 9. It can be seen from Figs. 7 to 9 that the three components are successfully separated and the proposed method has a high degree of decomposition accuracy. Then HVD and EMD are respectively applied to process the same signal. For HVD, the normalized filter cut-off frequency is set as 0.06. For EMD, eight IMFs are obtained, whereas just the second IMF, the third IMF and the fourth IMF represent the three harmonic components. Figs. 10 and 11 respectively illustrate the results obtained by the two methods. We can see from Fig. 10 that the component of 30 Hz is successfully separated, but the other two components are not rightly obtained owing to the noise interference. Although the EMD method effectively separates the three components, the accuracy of EMD is not finer than that of WRSD, and there are mixed modes in some time intervals (Fig. 11).

To investigate the influence of noise level, we increase the noise standard deviation from 0.3 to 1.0. The waveform of this noisy harmonic signal and its decomposed result of WRSD are shown in Fig. 12, and the errors between the original components and the obtained components are shown in Fig. 13. From Figs. 12 and 13, we can easily see that the decomposition accuracy of each component are decreased, especially the third component at the time interval [0, 0.9] s are not correctly decomposed. If the

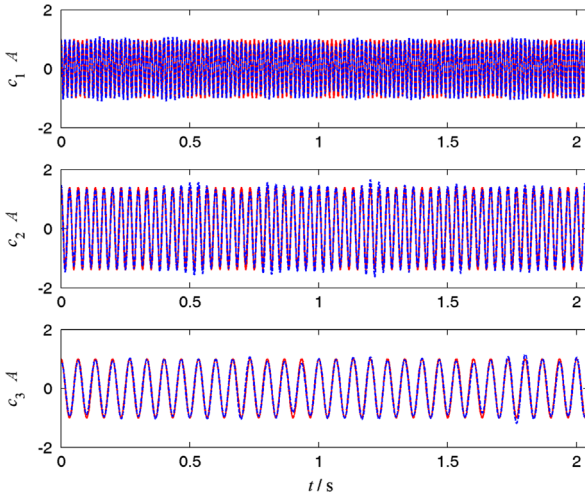


Fig. 7. The decomposed result of a noisy three-component harmonic signal obtained by WRSD, where the original component (—), the decomposed component (---).

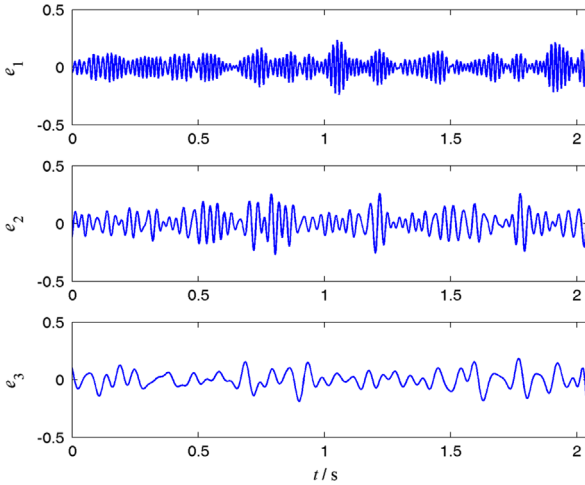


Fig. 8. The decomposed errors of a noisy three-component harmonic signal obtained by WRSD.

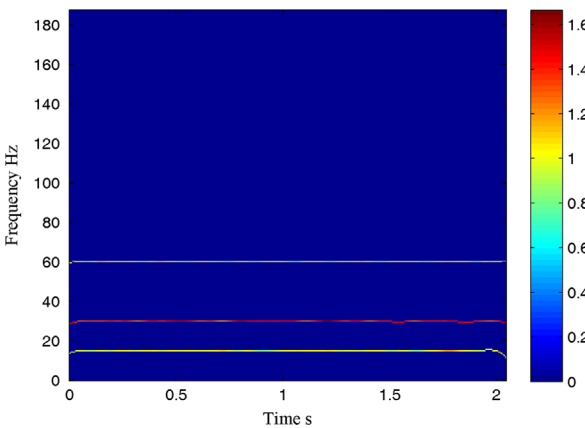


Fig. 9. The time–frequency spectrum of a noisy three-component harmonic signal obtained by WRSD.

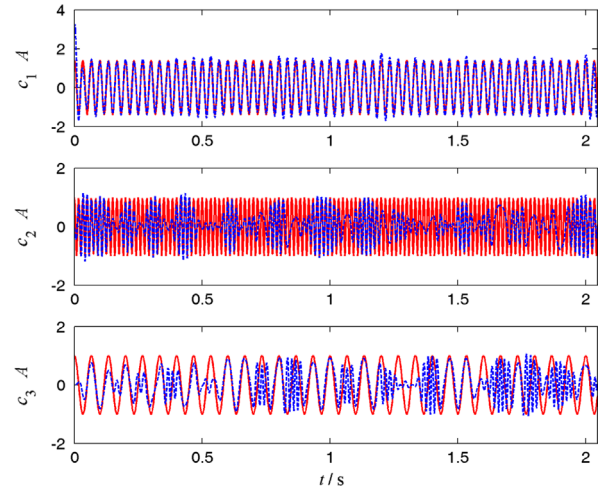


Fig. 10. The decomposed result of a noisy three-component harmonic signal obtained by HVD, where the original component (—), the decomposed component (---).

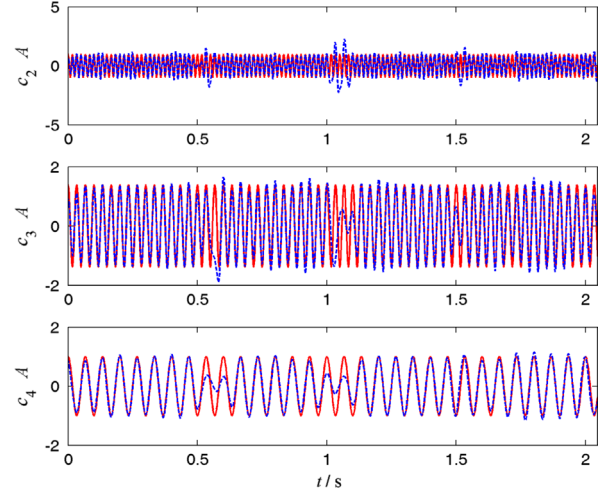


Fig. 11. The decomposed result of a noisy three-component harmonic signal obtained by EMD, where the original component (—), the decomposed component (---).

noise is too strong, other denoising technologies may be done first and then WRSD is performed, so as to improve the decomposition performance.

5.2. Example 2

To explain the influence of the number of components on the decomposability of WRSD, we use a noisy four-component harmonic signal for testing, which is given by

$$\begin{aligned} s(t) &= s_1(t) + s_2(t) + s_3(t) + s_4(t) + n_s(t) \\ &= 0.9 \cos(2\pi \times 90t - \pi/6) + \cos(2\pi \times 60t + \pi/4) \\ &\quad + 1.4 \cos(2\pi \times 30t + \pi/3) + \cos(2\pi \times 15t) + n_s(t) \end{aligned} \quad (34)$$

where $n_s(t)$ is a Gaussian white noise with the standard deviation of 0.2. To check the effect of sampling frequency, the sampling frequency is increased from 500 to 1000 Hz, and the length of signal is 2048.

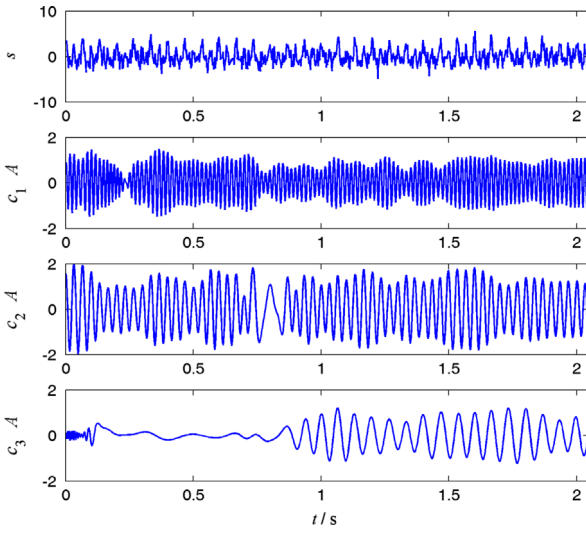


Fig. 12. The waveform of the strongly noisy three-component harmonic signal and its decomposed result of WRSD.

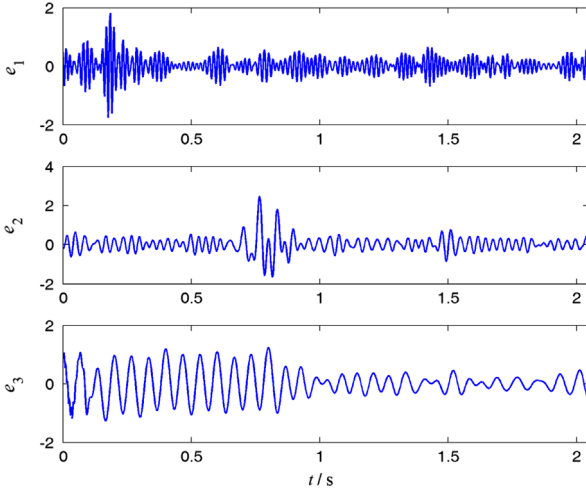


Fig. 13. The decomposed errors of a strongly noisy three-component harmonic signal obtained by WRSD.

The waveform of this noisy harmonic signal and its decomposed result of WRSD are illustrated in Fig. 14. The errors between the original components and the obtained components are shown in Fig. 15. To quantify the decomposability, we have calculated the error variances, mean square errors (MSE) and correlation coefficients (CC) between the original components and the obtained components, which are respectively listed in Table 1. From Fig. 15 and Table 1, we can see that the noisy four-component harmonic signal is correctly decomposed by WRSD and each obtained component has a small error compared to the corresponding original component. The experiment result shows that the number of components and sampling frequency has little impact on the proposed decomposition algorithm. Moreover, even if each component has different phases, the proposed method can still work well.

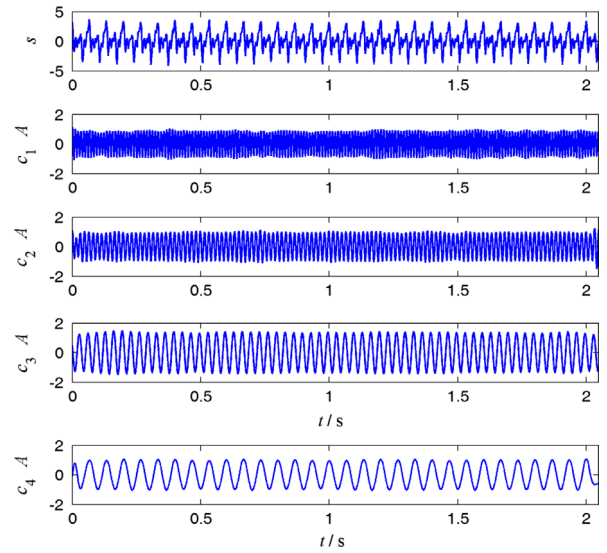


Fig. 14. The waveform of the noisy four-component harmonic signal and its decomposed result of WRSD.

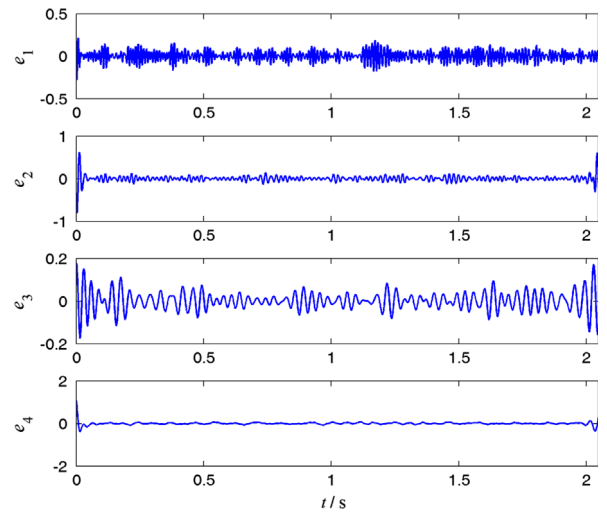


Fig. 15. The decomposed errors of a noisy four-component harmonic signal obtained by WRSD.

5.3. Example 3

When an external periodic force is applied to a linear vibration system, the total general response of the system with the external force is the superposition of the steady state and particular solutions. Signal decomposition method can be used to separate the two states. Suppose that the exciting force is a chirp force, then the noisy vibration response is given by

$$\begin{aligned} s(t) = & s_1(t) + s_2(t) = (0.8 - 0.175t^2) \\ & \times \cos(2\pi \times 15t) + (1 - 0.16t^2) \\ & \times \cos(2\pi \times 30t + 2\pi \times 5t^2) + n_s(t) \end{aligned} \quad (35)$$

where $n_s(t)$ is a Gaussian white noise with the standard deviation of 0.2. The sampling frequency is also 500 Hz,

Table 1

The measure indexes of the decomposed result in Example 2.

Measure index	$s_1(t)$	$s_2(t)$	$s_3(t)$	$s_4(t)$
Error variance	0.0033	0.0055	0.0018	0.0041
MSE	0.0033	0.0055	0.0018	0.0042
CC	0.9959	0.9945	0.9991	0.9959

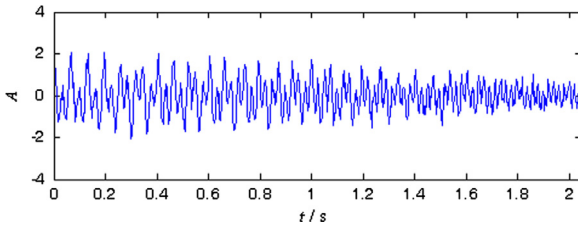


Fig. 16. The waveform of a noisy non-stationary vibration.

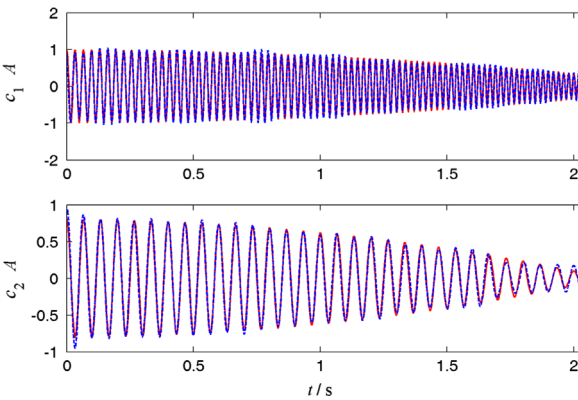


Fig. 17. The decomposed result of a noisy non-stationary vibration obtained by WRSD, where the original component (—), the decomposed component (---).

and the time interval is [0, 2.046] s. The waveform of this signal is illustrated in Fig. 16.

In this simulation, the same mother wavelet is used. The two components obtained by WRSD are shown in Fig. 17. Similarly, we calculate time–frequency spectrum of the decomposed result, which is shown in Fig. 18. It can be seen from Figs. 17 and 18 that the two vibration components are accurately extracted. We set the normalized filter cut-off frequency of HVD as 0.04, the result of HVD is shown in Fig. 19. The result obtained by EMD has seven IMFs, but just the second IMF and the third IMF respectively represent the two components $s_1(t)$ and $s_2(t)$, which are shown in Fig. 20. By comparing Figs. 17, 19 and 20, we can know that the WRSD method has the highest decomposition accuracy although the three methods successfully separate the two components. To further demonstrate the superiority of the proposed method, Table 2 lists the error variances, mean square errors (MSE) and correlation coefficients (CC) between the original components and the components obtained by the three methods, respectively. It again proves that the proposed method has the best decomposing accuracy. Moreover, at

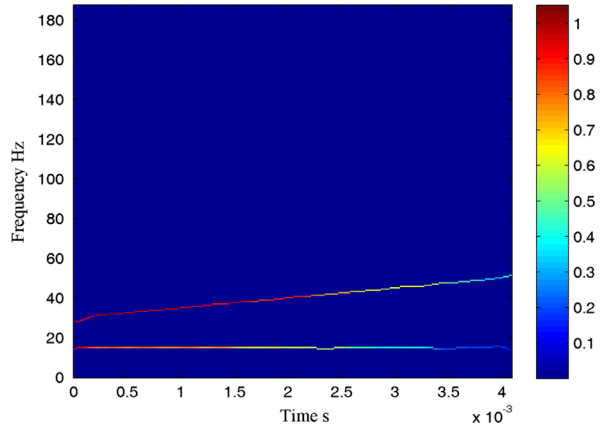


Fig. 18. The time–frequency spectrum of a noisy non-stationary vibration obtained by WRSD.

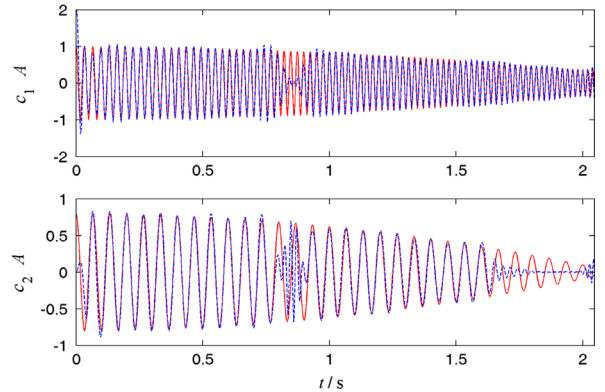


Fig. 19. The decomposed result of a noisy non-stationary vibration obtained by HVD, where the original component (—), the decomposed component (---).

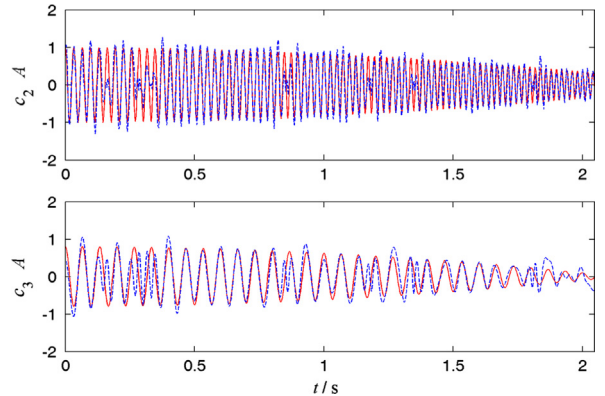


Fig. 20. The decomposed result of a noisy non-stationary vibration obtained by EMD, where the original component (—), the decomposed component (---).

the Matlab platform, we count the computation times of WRSD, HVD and EMD, which are respectively 1.9139, 1.4204 and 0.1019 s. As WRSD has the largest calculation amount, its calculation efficiency is the lowest, however the computation time is acceptable.

5.4. Example 4

The vibration signals of faulty rotating machineries, such as faulty gearboxes and bearings, are usually multicomponent amplitude modulation (AM) and phase modulation (FM) signals. To extract the faulty feature, it need calculate the modulation frequencies of some components, thus signal decomposition is an effective technology. Let us consider such a simulated multicomponent AM–FM signal that

$$x(t) = x_1(t) + x_2(t) + x_3(t) + n_s(t) \quad (36)$$

$$x_1(t) = [0.8 + 0.4 \sin(2\pi \times 10t)] \cos[2\pi \times 400t + \sin(2\pi \times 20t)] \quad (37)$$

$$x_2(t) = [1 + 0.3 \sin(2\pi \times 10t)] \cos[2\pi \times 200t + \sin(2\pi \times 10t)] \quad (38)$$

Table 2

The comparison of the three methods in Example 3.

Measure index	WRSD		HVD		EMD	
	$s_1(t)$	$s_2(t)$	$s_1(t)$	$s_2(t)$	$s_1(t)$	$s_2(t)$
Error variance	0.0024	0.0023	0.0233	0.0305	0.0552	0.0784
MSE	0.0024	0.0023	0.0233	0.0305	0.0554	0.0783
CC	0.9963	0.9939	0.9639	0.9121	0.9147	0.7920

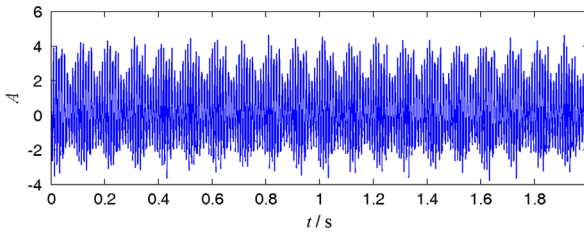


Fig. 21. The waveform of a noisy multicomponent AM–FM signal.

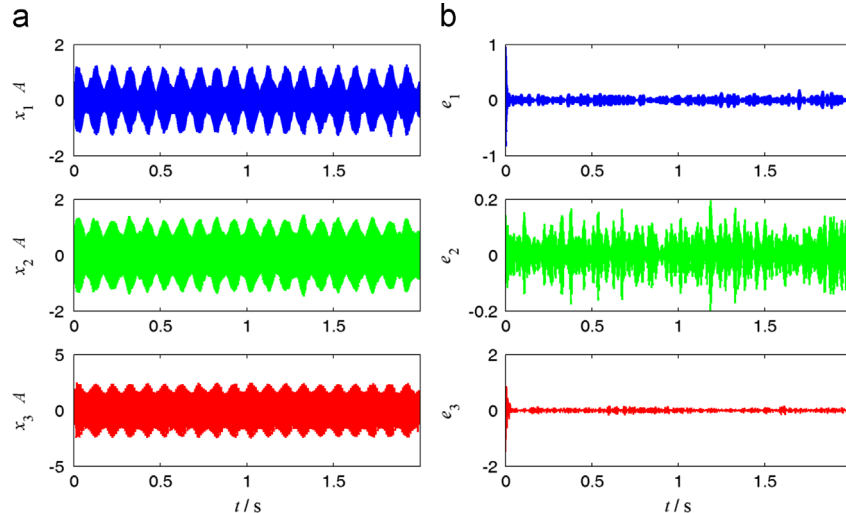


Fig. 22. The decomposed result of a noisy multicomponent AM–FM signal obtained by WRSD: (a) decomposed components; (b) decomposed error.

$$x_3(t) = [2 + 0.4 \cos(2\pi \times 10t)] \cos[2\pi \times 100t + \sin(2\pi \times 10t)] \quad (39)$$

where $n_s(t)$ is a Gaussian white noise with the standard deviation of 0.3. The sampling frequency is 2048 Hz, and the time interval is [0, 1.995] s. The time domain waveform of this simulated signal is illustrated in Fig. 21.

Similarly, the WRSD method is first used to decompose this signal, but the central frequency of the complex Morlet wavelet is chosen as 3π . The three obtained components and the errors between the original components and the components obtained by WRSD are respectively shown in Fig. 22(a) and (b). The corresponding time–frequency spectrum is shown in Fig. 23. It can be seen from Figs. 22 and 23 that the three components are effectively separated, whereas the error is relatively large at the ends of the first obtained component and the third obtained component. Then HVD and EMD are respectively applied to analyze this multicomponent AM–FM signal. The normalized filter cut-off frequency of HVD is set as 0.07, and the three components obtained by HVD and their errors are respectively shown in Fig. 24(a) and (b). It can be seen from Fig. 24 that the three components are not rightly separated at many time intervals and the decomposition accuracy is not fine. After EMD, ten IMFs are obtained, and the first IMF, the second IMF and the third IMF are respectively regarded as the three components $x_1(t)$, $x_2(t)$ and $x_3(t)$. The three IMFs and their errors are respectively shown in Fig. 25(a) and (b). From Fig. 25, we can see that the component $x_1(t)$ is not effectively separated and the other two IMFs also have large difference with $x_2(t)$ and $x_3(t)$. By comparing Figs. 22, 24 and 25, we can note that the WRSD method successfully decompose the simulated signal while HVD and EMD are difficult to exactly separate the three components. Moreover, it can be noted that HVD will first extract the largest energy component while WRSD and EMD will extract the component with the highest frequency. The error variances, mean square errors (MSE) and correlation coefficients (CC) between the original components and the components obtained by the

three methods are listed in Table 3, respectively. The comparative result further validates the superiority of the proposed method to HVD and EMD. Similarly, we also count the computation times of WRSD, HVD and EMD for processing the same multicomponent AM-FM signal, which are respectively 3.9858, 2.4256 and 0.1842 s. It can be also seen that EMD has the highest calculation efficiency among the three methods.

6. Application into mechanical fault diagnosis

To validate the feasibility of the proposed method in the mechanical engineering, it is applied to the fault diagnosis of flue gas turbine shaft and gearbox. Firstly, a vibration signal is sampled from a flue gas turbine shaft with misalignment fault by eddy current transducer. The sampling frequency is 500 Hz, and the rotating speed of the shaft is 996 rpm, i.e. the rotating frequency f_r is 16.6 Hz. The time domain waveform of the sampled signal is illustrated in Fig. 26. The WRSD method is used to

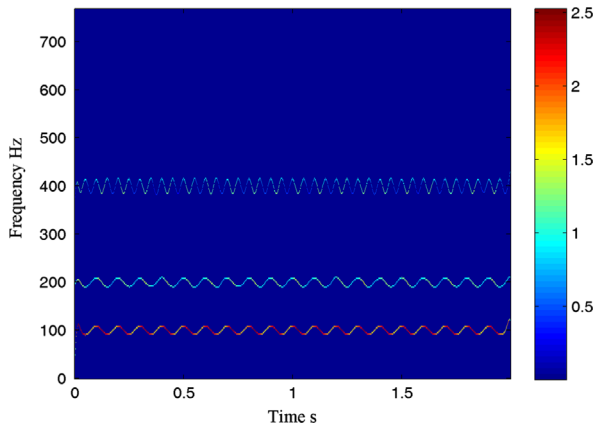


Fig. 23. The time–frequency spectrum of a noisy multicomponent AM–FM signal obtained by WRSD.

process the faulty vibration signal, and the central frequency of the complex Morlet wavelet is chosen as 4π . Two components are obtained, which are illustrated in Fig. 27. With the obtained IFs and IAs, we get the corresponding time–frequency spectrum, which is shown in Fig. 28. From this figure, we can clearly see that there are two spectral lines at f_r and $2f_r$. It illustrates that there is a misalignment fault in the shaft. The time–frequency spectra obtained by HVD and EMD are respectively shown in Figs. 29 and 30. For HVD, its normalized filter cut-off frequency is set as 0.06. It can be seen from Fig. 29 that there is mixing phenomenon between the rotating frequency component and its frequency doubling component. And from Fig. 30, we can see that the fault characteristic frequency (i.e. double rotating frequency) curve is very obscure. Therefore, the proposed method can more accurately achieve misalignment fault diagnosis than HVD and EMD.

Secondly, we employ the proposed method to diagnose a faulty gearbox. If a gear has a local fault, such as wear, crack, tooth break, etc., when the gear is meshing, the impulsive force caused by the damage will cause the variation of vibration amplitude and phase, i.e. generate AM and FM. Particularly when the fault characteristics are weak, the signal containing the fault characteristics is usually drowned by the background signals relevant to the rotary speed of the shaft and the conventional envelope spectrum analysis becomes inefficient. In such case, the envelope spectrum analysis method should be combined with the signal decomposition approach.

A faulty two-stage gearbox is used for experiment, and the teeth numbers of gears 1, 2, 3, 4 are respectively 30, 69, 18 and 81. The gear of output shaft has wear fault. The rotating speed of the input shaft is 2620 rpm, i.e. the rotating frequency of input shaft can be calculated as 43.67 Hz. It follows that fault characteristic frequency f_c is calculated as 4.22 Hz. The vibration signal is sampled by the accelerometer on the gearbox shell. The sampling frequency is 15,000 Hz, and the sampled vibration acceleration signal is illustrated in Fig. 31. The envelope

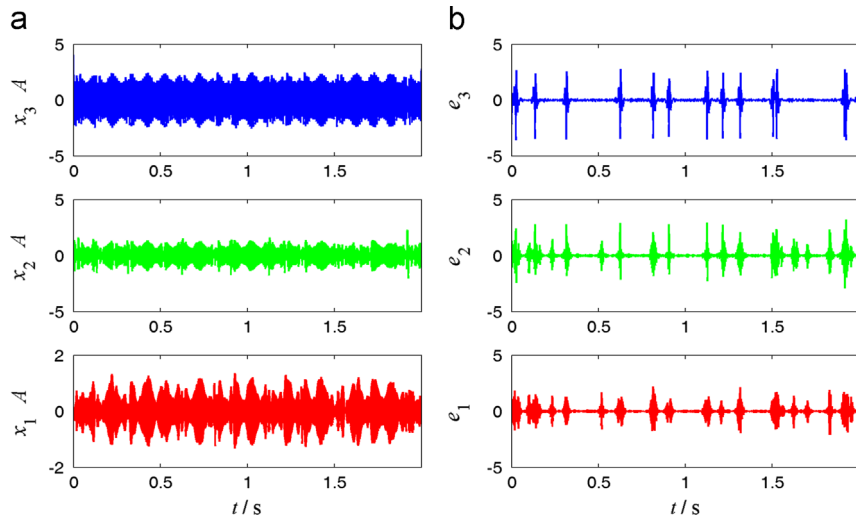


Fig. 24. The decomposed result of a noisy multicomponent AM–FM signal obtained by HVD: (a) decomposed components; (b) decomposed error.

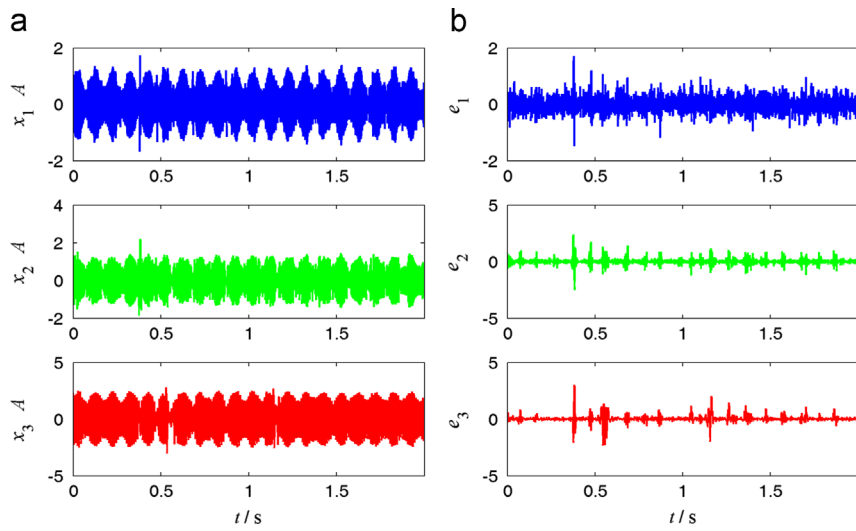


Fig. 25. The decomposed result of a noisy multicomponent AM–FM signal obtained by EMD: (a) decomposed components; (b) decomposed error.

Table 3

The comparison of the three methods in Example 4.

Measure index	WRSD			HVD			EMD		
	$x_1(t)$	$x_2(t)$	$x_3(t)$	$x_1(t)$	$x_2(t)$	$x_3(t)$	$x_1(t)$	$x_2(t)$	$x_3(t)$
Error variance	0.0039	0.0031	0.0091	0.0233	0.2503	0.2236	0.0595	0.0727	0.0971
MSE	0.0039	0.0031	0.0091	0.0233	0.2502	0.2235	0.0595	0.0727	0.0980
CC	0.9947	0.9971	0.9978	0.9639	0.9373	0.7720	0.9245	0.9301	0.9761

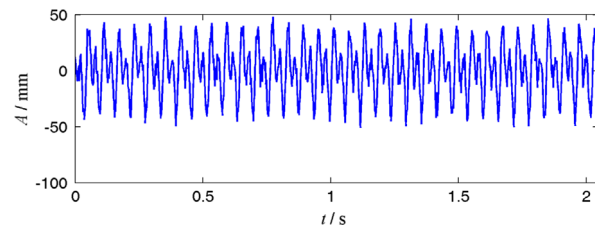


Fig. 26. The time domain waveform of a misalignment fault vibration signal.

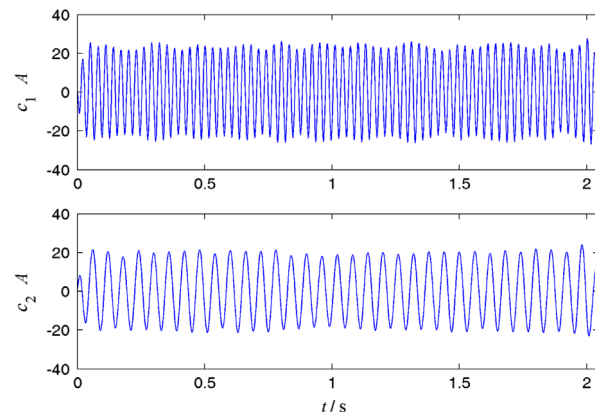


Fig. 27. The decomposed result of a misalignment fault vibration signal obtained by WRSD.

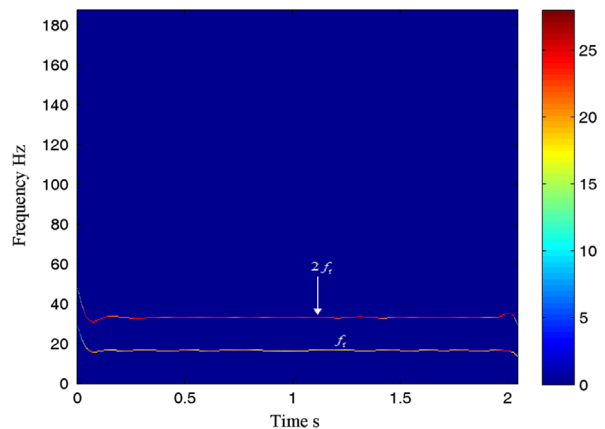


Fig. 28. The time–frequency spectrum of a misalignment fault vibration signal obtained by WRSD.

spectrum of this faulty vibration signal is illustrated in Fig. 32. Since the characteristic frequency is small, the analyzed frequency range is [0, 100] Hz in this example. From Fig. 32, we can see that there is not a clear spectral line at the fault characteristic frequency f_c whereas there is an obvious spectral line at the rotating frequency of input shaft. It immediately follows that the envelope spectrum analysis method loses efficacy. Thus, the WRSD method is employed to decompose this vibration signal, and the same complex Morlet wavelet is used. The first four

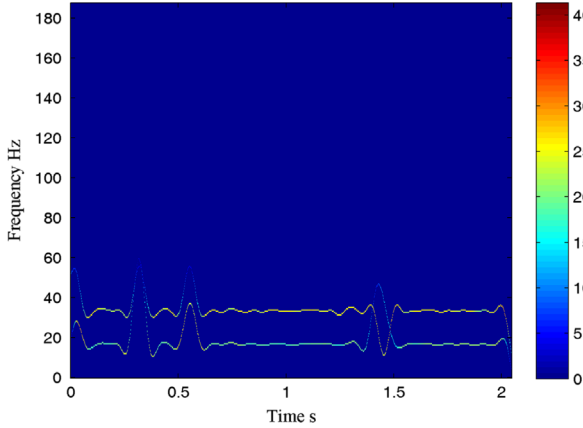


Fig. 29. The time–frequency spectrum of a misalignment fault vibration signal obtained by HVD.

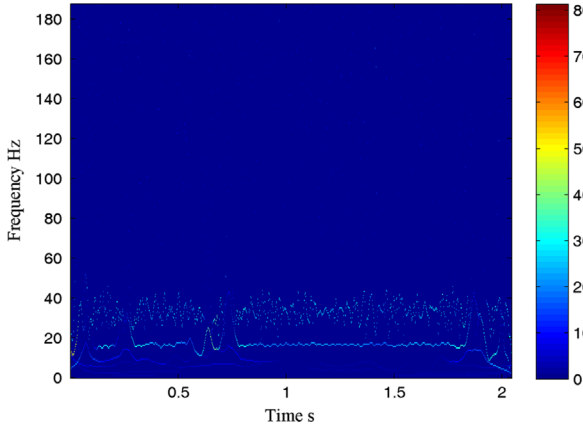


Fig. 30. The time–frequency spectrum of a misalignment fault vibration signal obtained by EMD.

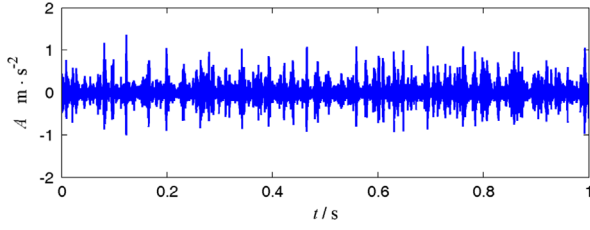


Fig. 31. The time domain waveform of a faulty gearbox vibration signal.

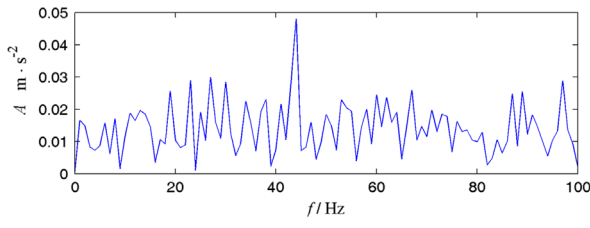


Fig. 32. The envelope spectrum of a faulty gearbox vibration signal.

components are shown in Fig. 33. Then the envelope spectra of the four components are calculated, which are respectively shown in Figs. 29–32. Obviously, there is no

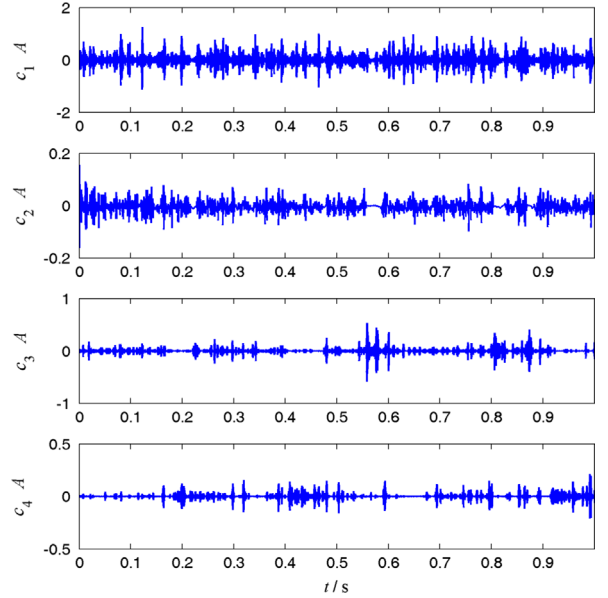


Fig. 33. The decomposed result of a faulty gearbox vibration signal obtained by WRSD.

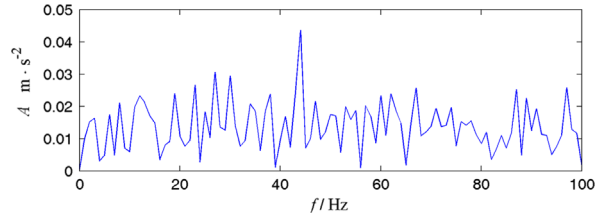


Fig. 34. The envelope spectrum of the first component obtained by WRSD.

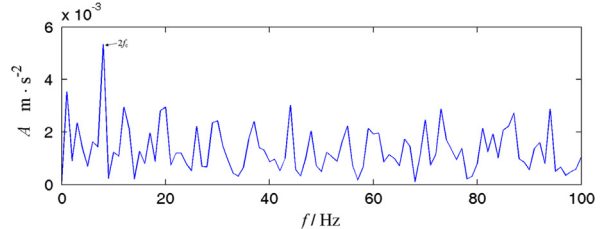


Fig. 35. The envelope spectrum of the second component obtained by WRSD.

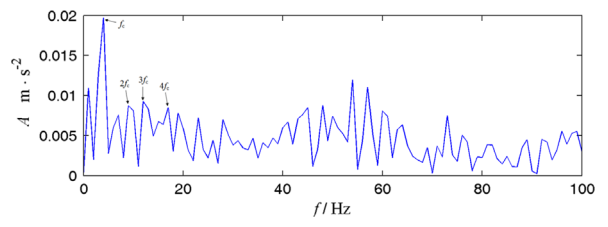


Fig. 36. The envelope spectrum of the third component obtained by WRSD.

clear characteristic spectral line in Fig. 34. It can be seen from Fig. 35 that there is a clear spectral line at the double characteristic frequency $2f_c$. And the third and fourth

components are the fault characteristic signals. Both Figs. 36 and 37 have clear spectral lines at the characteristic frequency f_c . Besides, Fig. 36 has spectral lines at the multiple characteristic frequencies $2f_c$, $3f_c$ and $4f_c$. The characteristic frequencies in Figs. 36 and 37 provide sufficient evidence for the existence of gear fault of the output shaft. HVD and EMD are also used for comparison. Similarly, we calculate the envelope spectra of the four components obtained by HVD and EMD, respectively. The result of HVD is illustrated in Fig. 38. From this figure, we find that only the envelope spectrum of the fourth component has an indistinctive spectral line at the double characteristic frequency $2f_c$. The result of EMD is illustrated in Fig. 39. It can be also found that only the envelope spectrum of the fourth component has a spectral line at $2f_c$. Therefore, for this faulty gearbox, HVD and EMD cannot identify the weak gear wear fault while WRSD can.

7. Conclusions

An adaptive and automatic multicomponent signal decomposition approach (WRSD) based on wavelet ridge extraction has been firstly developed in this paper. The used wavelet ridge extraction approach is based on the phase information of the wavelet coefficients, and it can

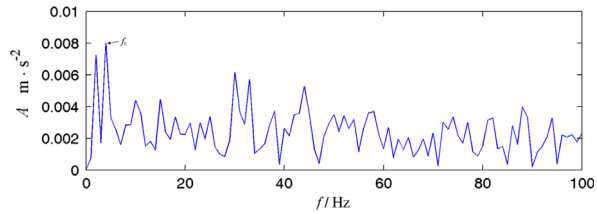


Fig. 37. The envelope spectrum of the fourth component obtained by WRSD.

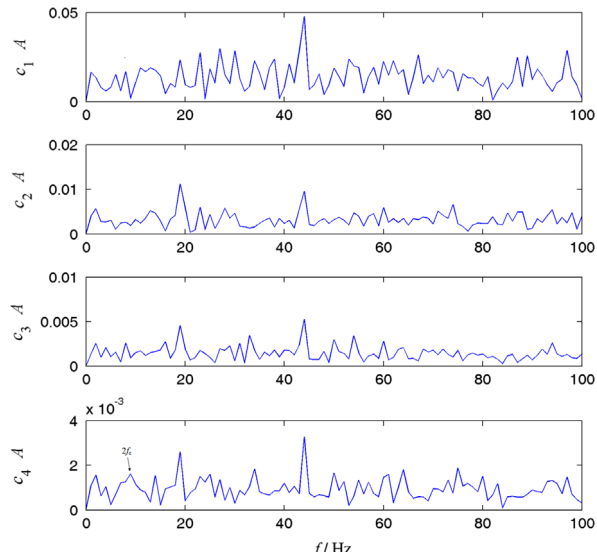


Fig. 38. The envelope spectra of the first four components obtained by HVD.

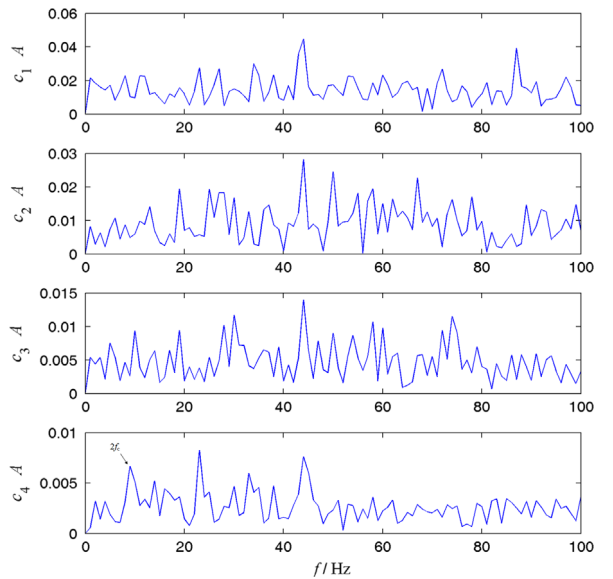


Fig. 39. The envelope spectra of the first four components obtained by EMD.

adaptively extract the ridge of one component, which depends on the initial scale. To overcome the problem of divergence in the iterative process, an improved wavelet ridge extraction algorithm is used to extract the IF of one component and then the corrected IF is obtained by low-pass filtering. After obtaining the IF of one component, the conventional synchronous demodulation method is used to separate this component from the multicomponent signal. In this process, the estimation of the IF is very important for the decomposition accuracy. Due to the fine time-frequency localization property of wavelet transform, the IF estimation in WRSD has high accuracy and anti-noise performance, thus it results in that the proposed WRSD method is very accurate and less sensitive to the noise. The effectiveness and advantage of WRSD is validated by three typical simulated vibration signals including stationary signals and nonstationary signals, and it has been successfully applied to mechanical fault diagnosis.

Since the parameter of the asymptotic analytic wavelet is related to the accuracy and resolution of ridge extraction, we can optimize the wavelet parameter at each iteration to further improve the decomposition performance of the proposed WRSD. This is the extension and development of this work.

Acknowledgments

The work described in this paper was supported by the Fundamental Research Funds for the Central Universities (No. CDJZR14285501), China Postdoctoral Science Foundation funded project (No. 2012M521690), Natural Science Foundation Project of CQCSTC (cstc2012jjA70003), and National Natural Science Foundation of China (Nos. 50905191 and 51435001). The authors also thank the

anonymous reviewers for their valuable comments that helped improve this paper.

Appendix A

Firstly, let us consider such case that $C(a) < 1$. Note that the Fourier transform of window function of the Morlet wavelet is a real function. From Eq. (20), we have

$$\psi(a, b) = \omega_1 b + \arctan \frac{\sin [(\omega_2 - \omega_1)b + \varphi]}{1 + C(a) \cos [(\omega_2 - \omega_1)b + \varphi]} \quad (\text{A.1})$$

Let $\theta = (\omega_2 - \omega_1)b + \varphi$, then the derivative of $\psi(a, b)$ is calculated as

$$\frac{\partial \psi(a, b)}{\partial b} = \omega_1 + \frac{[\cos \theta + C(a)](\omega_2 - \omega_1)}{2 + C(a) \cos \theta + [C^2(a) - 1] \cos^2 \theta} \quad (\text{A.2})$$

From Eq. (23), we have

$$\begin{aligned} \omega_a &= \omega_1 + \frac{1}{T} \int_{b_0}^{b_0+T} \frac{[\cos \theta + C(a)](\omega_2 - \omega_1)}{2 + C(a) \cos \theta + [C^2(a) - 1] \cos^2 \theta} d\theta \\ &= \omega_1 + \frac{1}{T} \int_{\theta_0}^{\theta_1} \frac{\cos \theta + C(a)}{2 + C(a) \cos \theta + [C^2(a) - 1] \cos^2 \theta} d\theta \end{aligned} \quad (\text{A.3})$$

where $\theta_0 = (\omega_2 - \omega_1)b_0 + \varphi$ and $\theta_1 = (\omega_2 - \omega_1)(b_0 + T) + \varphi$. By using partial fraction expansion, we can write

$$\frac{\cos \theta + C(a)}{2 + C(a) \cos \theta + [C^2(a) - 1] \cos^2 \theta} = \frac{A_1}{\cos \theta + x_1} + \frac{A_2}{\cos \theta + x_2} \quad (\text{A.4})$$

where

$$x_{1,2} = \frac{C(a) \pm \sqrt{2 - C^2(a)}}{C^2(a) - 1} \quad (\text{A.5})$$

When $C(a) < 1$, it can be proven that $(x_{1,2})^2 > 1$. Then from Eqs. (A.3) and (A.4), the error can be written as

$$\begin{aligned} e &= \frac{1}{T} \int_{\theta_0}^{\theta_1} \frac{\cos \theta + C(a)}{2 + C(a) \cos \theta + [C^2(a) - 1] \cos^2 \theta} d\theta \\ &= \frac{1}{T} \left[\frac{2A_1}{x_1 + 1} \sqrt{\frac{x_1 + 1}{x_1 - 1}} \arctan \left(\sqrt{\frac{x_1 - 1}{x_1 + 1}} \tan \frac{\theta}{2} \right) \right. \\ &\quad \left. + \frac{2A_2}{x_2 + 1} \sqrt{\frac{x_2 + 1}{x_2 - 1}} \arctan \left(\sqrt{\frac{x_2 - 1}{x_2 + 1}} \tan \frac{\theta}{2} \right) \right] \Big|_{\theta_0}^{\theta_1} \end{aligned} \quad (\text{A.6})$$

The above definite integral mainly depends on $\tan \frac{\theta}{2}|_{\theta_0}^{\theta_1}$, which is calculated as

$$\tan \frac{\theta}{2} \Big|_{\theta_0}^{\theta_1} = \frac{\sin [(\omega_2 - \omega_1)T/2]}{\cos \theta_0 \cos \theta_1} = \frac{\sin (n\pi + \varepsilon/2)}{\cos \theta_0 \cos \theta_1} \quad (\text{A.7})$$

when ε is small enough, $|\sin(n\pi + \varepsilon/2)|$ can be approximated by $\varepsilon/2$. Moreover, we can see from Eq. (22) that T mainly depends on n . It then follows from Eqs. (A.6) and (A.7) that the error is proportional to ε/n . Thus Eq. (24) holds.

Secondly, we consider the case that $C(a) > 1$. Eq. (20) needs to be rewritten as

$$W_s(a, b) = A_2 \bar{G}(a\omega_2) e^{i\omega_2 b} \left[1 + C'(a) e^{i(\omega_1 - \omega_2)b + i\varphi} \right] \quad (\text{A.8})$$

where

$$C'(a) = \frac{A_1 \bar{G}(a\omega_1)}{A_2 \bar{G}(a\omega_2)} = \frac{1}{C(a)} \quad (\text{A.9})$$

Obviously, we have $C'(a) < 1$. With the similarly approach, Eq. (24) can be proven. Ref. [22] also gives the similarly result, but the derivation was not given.

References

- [1] L. Cohen, Time–Frequency Analysis, Prentice-Hall, New York, 1995.
- [2] S. Qian, D. Chen, Decomposition of the Wigner–Ville distribution and time–frequency distribution series, IEEE Trans. Signal Process. 42 (1994) 2836–2842.
- [3] Z.K. Peng, F.L. Chu, Y.Y. He, Vibration signal analysis and feature extraction based on reassigned wavelet scalogram, J. Sound Vib. 253 (5) (2002) 1087–1100.
- [4] Y. Qin, S.R. Qin, Y.F. Mao, Research on iterated Hilbert transform and its application in mechanical fault diagnosis, Mech. Syst. Signal Process. 22 (8) (2008) 1967–1980.
- [5] Y.G. Lei, J. Lin, Z.J. He, M.J. Zuo, A review on empirical mode decomposition in fault diagnosis of rotating machinery, Mech. Syst. Signal Process. 35 (2013) 108–126.
- [6] Y. Qin, B. Tang, J. Wang, K. Xiao, A new method for multicomponent signal decomposition based on self-adaptive filtering, Measurement 44 (7) (2011) 1312–1327.
- [7] M. Feldman, Hilbert transform methods for nonparametric identification of nonlinear time varying vibration systems, Mech. Syst. Signal Process. 47 (2014) 66–77.
- [8] C. Chen, S.M. Guo, W.S. Chang, J.S.H. Tsai, K.S. Cheng, An improved bidimensional empirical mode decomposition: a mean approach for fast decomposition, Signal Process. 47 (2014) 66–77.
- [9] W.L. Hwang, J. Ho, Null space component analysis for noisy blind source separation, Signal Process. 109 (2015) 301–316.
- [10] S. Mallat, A Wavelet Tour on Signal Processing, Academic Press, New York, 1998.
- [11] Y. Qin, B.P. Tang, J.X. Wang, Higher-density dyadic wavelet transform and its application, Mech. Syst. Signal Process. 24 (3) (2010) 823–834.
- [12] Y. Qin, J.X. Wang, Y.F. Mao, Dense framelets with two generators and their application in mechanical fault diagnosis, Mech. Syst. Signal Process. 40 (2) (2013) 483–498.
- [13] N.E. Huang, Z. Shen, S.R. Long, M.C. Wu, H.H. Shih, Q. Zheng, N.C. Yen, C.C. Tung, H.H. Liu, The empirical mode decomposition and Hilbert spectrum for nonlinear and nonstationary time series analysis, Proc. R. Soc. Lond.–Ser. A 454 (1998) 903–995.
- [14] R.T. Rato, M.D. Ortigueira, A.G. Batista, On the HHT, its problems, and some solutions, Mech. Syst. Signal Process. 22 (6) (2008) 1374–1394.
- [15] M. Feldman, Time-varying vibration decomposition and analysis based on the Hilbert transform, J. Sound Vib. 295 (3–5) (2006) 518–530.
- [16] S. Braun, M. Feldman, Decomposition of non-stationary signals into varying time scales: Some aspects of the EMD and HVD methods, Mech. Syst. Signal Process. 25 (7) (2011) 2608–2630.
- [17] G.D. Chen, Z.C. Wang, A signal decomposition theorem with Hilbert transform and its application to narrowband time series with closely-spaced frequency components, Mech. Syst. Signal Process. 28 (2012) 258–279.
- [18] S. Olhede, A.T. Walden, A generalized demodulation approach to time–frequency projections for multicomponent signals, Proc. R. Soc. A 461 (2005) 2159–2179.
- [19] J.S. Cheng, Y. Yang, D.J. Yu, Application of the improved generalized demodulation time–frequency analysis method to multi-component signal decomposition, Signal Process. 89 (2009) 1205–1215.
- [20] Z.P. Feng, F.L. Chu, M.J. Zuo, Time–frequency analysis of time-varying modulated signals based on improved energy separation by iterative generalized demodulation, J. Sound Vib. 330 (2011) 1225–1243.
- [21] Y. Qin, Y.F. Mao, B.P. Tang, Vibration signal component separation by iteratively using basis pursuit and its application in mechanical fault detection, J. Sound Vib. 332 (20) (2013) 5217–5235.
- [22] N. Delprat, B. Escudie, P. Guillemin, R. Kronland-Martinet, P. Tchamitchian, B. Torrksani, Asymptotic wavelet and Gabor analysis: extraction of instantaneous frequencies, IEEE Trans. Inf. Theory 38 (2) (1992) 644–664.
- [23] M. Feldman, Hilbert Transform Applications in Mechanical Vibration, John Wiley & Sons, New York, 2011.